Systems/Circuits

Distinct Representation and Distribution of Visual Information by Specific Cell Types in Mouse Superficial Superior Colliculus

Samuel D. Gale and Gabe J. Murphy
Howard Hughes Medical Institute/Janelia Farm Research Campus, Ashburn, Virginia 20147

The superficial superior colliculus (sSC) occupies a critical node in the mammalian visual system; it is one of two major retinorecipient areas, receives visual cortical input, and innervates visual thalamocortical circuits. Nonetheless, the contribution of sSC neurons to downstream neural activity and visually guided behavior is unknown and frequently neglected. Here we identified the visual stimuli to which specific classes of sSC neurons respond, the downstream regions they target, and transgenic mice enabling class-specific manipulations. One class responds to small, slowly moving stimuli and projects exclusively to lateral posterior thalamus; another, comprising GABAergic neurons, responds to the sudden appearance or rapid movement of large stimuli and projects to multiple areas, including the lateral geniculate nucleus. A third class exhibits direction-selective responses and targets deeper SC layers. Together, our results show how specific sSC neurons represent and distribute diverse information and enable direct tests of their functional role.

Key words: **retinorecipient; tectum**

Introduction

The profound visual deficits caused by lesions of the dorsal lateral geniculate nucleus (dLGN) or primary visual cortex (V1) in primates, and the large proportion of primate retinal ganglion cells that project to the dLGN relative to other retinorecipient areas (Perry and Cowey, 1984; Perry et al., 1984), motivated numerous studies focused on the organization and processing of visual information in the geniculocortical pathway (for review, see Livingstone and Hubel, 1988; Shapley, 1990; Merigan and Maunsell, 1993; Callaway, 1998; Nassi and Callaway, 2009). However, lesions of V1 do not abolish primates' ability to locate and/or distinguish visual stimuli (for review, see Weiskrantz, 2009; Cowey, 2010; Leopold, 2012). Moreover, in many mammals, inactivating V1 has only a modest effect on visually guided behavior (Schneider, 1969; Dean, 1981; Glickfeld et al., 2013). Residual visual function under these conditions likely reflects the fact that an equivalent (or greater) number of retinal ganglion cells target a region distinct from the dLGN in many vertebrates (Chalupa and Thompson, 1980; Vaney et al., 1981), i.e., the superficial layers of the superior colliculus (sSC; also known as the optic tectum).

sSC neurons could contribute to visually guided behavior in several different ways. First, the sSC projects directly to the dLGN (for review, see May, 2006); therefore, processing in the sSC can modify signals in the geniculocortical pathway. Second, the sSC projects to the lateral posterior nucleus of the thalamus (LP; also known as pulvinar), a nucleus that directly innervates several higher-order visual cortical areas (Tohmi et al., 2014). Third, sSC neurons provide visual input to (deeper) layers of the SC that facilitate selection of sensory targets, control of spatial attention, and/or movements of the eyes and head (for review, see Wurtz and Albano, 1980; Mysore and Knudsen, 2011; Krauzlis et al., 2013).

Determining the contribution of the sSC to downstream neural activity and visually guided behavior requires knowledge of the features of visual stimuli to which specific types of sSC neurons respond, the downstream areas to which these neurons project, and a means to manipulate the output of these cells. Therefore, we (1) distinguished several classes of neurons in the mouse sSC on the basis of their morphological and electrophysiological characteristics, (2) assayed the features of visual stimuli to which these classes of neurons respond, and (3) identified transgenic mice in which Cre recombinase is expressed in specific sSC cell types. This approach revealed four classes of sSC neurons that respond to distinct features of visual stimuli. Cell type-specific expression of fluorescent proteins and retrograde labeling revealed that each target of the sSC receives input from different subsets of cell types and thus information about some but not other features of visual stimuli.

Received July 8, 2014; revised Aug. 13, 2014; accepted Aug. 20, 2014.

Author contributions: S.D.G. and G.J.M. designed research; S.D.G. performed research; S.D.G. and G.J.M. analyzed data; S.D.G. and G.J.M. wrote the paper.

This work was supported by the Howard Hughes Medical Institute. We thank Monique Copeland, Amy Hu, Susan Michael, and Brenda Shields for help with tissue sectioning and histology, Sarah Lindo and Kendra Morris for surgical assistance, Mark Cafaro, Frank Midgley, and Barry Wark for help developing data acquisition software, Calin Culianu and Anthony Leonardo for sharing and modifying software for stimulus generation, Ben Sivyer for sharing LGN electrophysiology data, and Kevin Briggman, Gidon Felsen, Greg Horwitz, Rich Krauzlis, David Perkel, and Fred Rieke for comments on this manuscript.

The authors declare no competing financial interests.

Correspondence should be addressed to Gabe J. Murphy, Howard Hughes Medical Institute/Janelia Farm Research Campus, 19700 Helix Drive, Ashburn, VA 20147. E-mail: murphyg@janelia.hhmi.org.

DOI:10.1523/JNEUROSCI.2768-14.2014

 0270-6474/14/3413458-14$15.00/0

Materials and Methods

Mice. All procedures were approved by the Janelia Farm Institutional Animal Care and Use Committee. Mice of either sex were 6–16 weeks old at the time of all *in vitro* and *in vivo* electrophysiological recordings. For some experiments, we used the following transgenic mice: Gad2–Cre (Taniguchi et al., 2011), Gad2–Cre × Ai9 (Madisen et al., 2010), vGAT–ChR2 (Zhao et al., 2011), Ntsr1–GN209–Cre (Gerfen et al., 2013), and Grp–KH288–Cre (Gerfen et al., 2013).

Virus and fluorescent tracer injections. To express fluorescent proteins or channelrhodopsin-2 (ChR2) in a Cre-recombinase-dependent manner for *in vitro* recordings, we pressure injected 20 nl of AAV-2.1–Syn–FLEX–GFP or AAV-2.1–Syn–FLEX–ChR2–GFP into the sSC and prepared brain slices 4–6 weeks after virus injection. For Cre-dependent anterograde labeling, 10 nl of AAV-2.1–Cag–FLEX–tdTomato was injected in the sSC, and mice were perfused 2 weeks later. For *in vitro* recordings of retrogradely labeled cells, green retrobeads (Lumafuor; 1:1 dilution in PBS) or cholera toxin conjugated to Alexa Fluor 488 (1%; Invitrogen) were injected into one of the projection targets of the sSC, and slices were prepared 4–14 d later. Injection coordinates were as follows (anterior from lambda, lateral from midline, and depth; in mm): SC, 0–0.2, 0.3–0.8, and 0.8–1.2; parabigeminal nucleus (PBg), −0.2–0.2, 1.7–1.9, and 3.0–3.2; LP, 2.1–2.3, 1.7, and 2.1–2.3; dLGN, 1.7–1.8, 2.2–2.4, and 2.6–2.8; and ventral lateral geniculate nucleus (vLGN), 1.7–1.8, 2.3–2.5, and 3–3.2.

Injection of adeno-associated virus (AAV) can retrogradely label cells whose axons target the region injected; the number of retrograde labeled cells depends on the particular brain region and other factors (Harris et al., 2012; Wang et al., 2014). After sSC injections of virus encoding non-conditional fluorescent protein expression, we observed retrogradely labeled neurons in several regions known to provide input to the sSC: retina, layer 5 of visual cortex, and PBg. However, after sSC injections of virus encoding Cre-dependent fluorescent protein expression, we did not observe retrograde labeling in the three Cre lines used in this study, with one exception (PBg neurons in Ntsr1–GN209–Cre mice).

For one experiment, we took advantage of retrograde labeling by AAV to retrogradely label Cre-expressing sSC neurons in Gad2–Cre mice that project to the thalamus or PBg (see Results). We injected AAV-2.1–FLEX–CAG–GFP into thalamus or PBg and prepared slices for *in vitro* recordings of sSC neurons 10–14 d later.

Recordings in brain slices. Coronal or parasagittal slices, 400 μm thick, were cut with a vibratome (Leica) in chilled cutting solution containing the following (in mM): 60 sucrose, 83 NaCl, 25 $NaHCO_3$, 1.25 NaH_2PO_4, 2.5 KCl, 0.5 $CaCl_2$, 6 $MgCl_2$, 20 D-glucose, 3 Na pyruvate, and 1 ascorbic acid. Slices were transferred to warm (34°C) cutting solution, which was then allowed to cool to room temperature. Approximately 60 min after cutting, slices were transferred to ACSF containing the following (in mM): 125 NaCl, 25 $NaHCO_3$, 1.25 NaH_2PO_4, 2.5 KCl, 1.3 $CaCl_2$, 1 $MgCl_2$, 20 D-glucose, 3 Na pyruvate, and 1 ascorbic acid for recording (at 32°C) or additional storage (room temperature). Whole-cell, current-clamp recordings were made with glass pipettes filled with the following (in mM): 134 K-gluconate, 6 KCl, 4 NaCl, 10 HEPES, 2 MgATP, 0.4 NaGTP, 10 Tris phosphocreatine, and either 0.1 Na Alexa Fluor 488 hydrazide or 0.05 Na Alexa Fluor 594 hydrazide. Electrode resistance was 3–8 MΩ. Membrane voltage was amplified 50 times and low-pass filtered (4 kHz cutoff) with a Multiclamp 700B amplifier (Molecular Devices) and digitized at 50 kHz with an ITC-18 data acquisition interface (HEKA). Data acquisition was controlled using open source software (http://symphony-das.github.io/). ChR2 was activated with LED flashes (455 nm peak emission) delivered through a 63× objective. In some experiments, one or more drugs were applied via the ACSF perfusing the slice (all drugs purchased from Tocris Bioscience): the AMPA receptor antagonist NBQX (10 μM), the NMDA receptor antagonist AP-5 (50 μM), the $GABA_A$ receptor antagonist gabazine (10 μM), the Na^+-channel blocker TTX (1 μM), or the K^+-channel blocker 4-AP (100 μM). At the end of recordings, fluorescently filled cells were imaged with a two-photon microscope (Prairie) using 880–920 nm excitation light.

In vivo *recordings, visual stimuli, and single-cell electroporation.* Mice were anesthetized via intraperitoneal injection of urethane (1.5 g/kg). A craniotomy was made over the right SC, and a plastic head holder was attached to the skull. Body temperature was maintained with a warm blanket under the animal. A patch electrode (same as above) filled with 0.9% NaCl and 1–1.5% Neurobiotin was lowered into the right SC. Current pulses were used to monitor changes in pipette resistance. When a cell was encountered, pipette pressure (20–30 mbar) was released and a loose seal (<20 MΩ) formed. Extracellular voltage signals were acquired using the same equipment and software as above for whole-cell recordings, except that a 100 Hz high-pass filter was also applied and data were sampled at 20 kHz.

Visual stimuli were generated with StimGL software (Calin Culianu and Anthony Leonardo, Janelia Farm Research Campus, Ashburn, VA) and projected on a screen at 120 frames/s with a modified digital light processing projector and SugarCube LED illuminator. The screen was 12.1 cm from the mouse's left eye and subtended 15–100° laterally from directly in front of the mouse and 10° below and 40° above the mouse's eye. Stimuli included stationary or moving light spots (48.4 cd/m^2) on a dark background (0.2 cd/m^2) or drifting sinusoidal gratings (with the same maximum and minimum luminance; Michelson contrast 99.2%).

At the end of recordings, Neurobiotin was electroporated into the cell. Positive current pulses were applied at 2 Hz with a 50% duty cycle and increasing amplitude (0.5–8 nA) until the recorded cell began to fire action potentials (APs) entrained to the current steps. When possible, we maintained entrainment for several minutes. Mice were perfused <30 min after electroporation. Parasagittal sections (50 μm) containing the right SC were cut with a vibratome. Neurobiotin cell fills were visualized with Alexa Fluor 488- or 594-conjugated streptavidin or 3,3′-diaminobenzidine tetrahydrochloride (DAB). Fluorescently labeled cell fills were imaged with a Zeiss confocal microscope; DAB-labeled cell fills were traced using a Neurolucida system.

Analysis of somatodendritic morphology. We used z-projections of images or tracings of filled cells to measure eight morphological properties that were used for clustering. The orientation of each cell was standardized by finding the point along the dorsal SC surface closest to the soma and defining the axis extending from the soma to this point as "vertical" and the axis orthogonal to this and intersecting the soma as "horizontal" (Fig. 1*A*) We refer to the space between the horizontal axis and the dorsal SC surface as "above" the soma and the space to the other side of the horizontal axis as "below" the soma. We measured the soma distance from the SC surface (parameter 1) and the horizontal width of the dendritic arbor (parameter 2). Sholl analysis (Sholl, 1953) was used to measure the number and location of dendritic branches; the number of dendrite intersections with circles of increasing radii from the center of the soma (25 μm increments) were counted (we refer to the intersections as Sholl points and the circles as Sholl radii). Drawing two perpendicular lines that intersect at the soma and are 45° offset from the vertical and horizontal axes divides the dendritic arbor into four quadrants: two vertical quadrants above and below the soma, respectively, and two horizontally extending quadrants (Fig. 1*A*). We calculated the dendritic "arbor orientation index" (parameter 3) as follows: (Sholl points in vertical quadrants − Sholl points in horizontal quadrants)/(total Sholl points). Arbors with an arbor orientation index near 1 are vertically oriented, arbors with an arbor orientation index near −1 are horizontally oriented, and arbors with dendrites branching equally in all directions have an arbor orientation index near 0. We determined the maximum number of Sholl points at a single radius (parameter 4), the Sholl radius at which this occurred (parameter 5), and the total number of Sholl points (parameter 6). We also measured the soma area (parameter 7) and the mean thickness of primary dendrites at 15 μm from the center of the soma (parameter 8).

Analysis of intrinsic electrophysiological properties. Changes in membrane potential in response to hyperpolarizing and depolarizing current steps (500 ms) were used to measure 11 intrinsic electrophysiological properties for clustering (Fig. 2). Current steps producing a small hyperpolarization (<5 mV) from the resting potential (parameter 1) were used to determine input resistance (parameter 2). Many neurons exhibit a slowly developing, depolarizing "sag" in response to hyperpolarizing current injection. We calculated the sag amplitude in two ways (parameters 3 and 4): we used traces in which the peak hyperpolarization in

response to negative current injection was near −90 mV or was 10 mV below resting potential and took the difference between the initial peak (near −90 mV or 10 mV below resting potential) and the "steady-state" potential near the end of the current step. The former traces (peak hyperpolarization near −90 mV) were also used to measure the time elapsed between the peak hyperpolarization and development of the sag to half of its maximum amplitude (parameter 5). APs in response to the minimum current required for AP generation were used to determine the AP threshold (the potential at which the temporal derivative of the membrane potential first exceeded 20 mV/ms; parameter 6), AP duration (time between reaching AP threshold and then falling below this potential again after the AP peak; parameter 7), and afterpolarization amplitude (difference between AP threshold and the minimum potential after an AP; parameter 8). The amplitude of depolarizing current steps was increased until the neuron achieved or closely approached its maximum "sustained" firing rate. We calculated the maximum steady-state firing rate (parameter 9) as the average firing rate over the last 250 ms of the current step and the maximum peak firing rate (parameter 10) as the reciprocal of the shortest interspike interval. Some neurons had a sustained depolarization (sometimes accompanied by APs) after depolarizing current injection. We median filtered membrane potential traces (10 ms window) and determined the maximum spike-train afterdepolarization (ADP; parameter 11) between 200 and 300 ms after depolarizing current steps.

Cell-type clustering. For cluster analysis, each data parameter was standardized by subtracting the population mean and dividing by the SD. Clustering was performed in p-dimensional space, where p is the number of parameters, without any previous dimensionality reduction. We used Euclidean distances and Ward's linkage criterion for hierarchical clustering; results were nearly identical if we used k-means clustering.

We used two complementary methods to compare clusters derived using morphological or electrophysiological parameters (Fig. 2*E*,*F*). The first method, the adjusted Rand index (Rand, 1971; Hubert and Arabie, 1985), ignores the problem of how to match clusters from one set of parameters (morphology) to those from the other set (electrophysiology). Instead, the Rand index counts the fraction of cell pairs that were clustered together or apart for both parameter sets and then corrects for chance similarity (alternatively, a pair of cells could be clustered together using the morphological parameters but separately using the electrophysiological parameters or vice versa).

A potential disadvantage of comparing two sets of clusters with the Rand index is that a small cluster derived using one type of parameter (e.g., morphology) will only have a small effect on the value of the Rand index, even if that cluster is very different from all clusters derived using the other type of parameter (e.g., electrophysiology). We used a second measure (number of noncorresponding clusters) that addresses this issue by using a simple rule to match each electrophysiology cluster with one morphology cluster: for each electrophysiology cluster, the matching morphology cluster is the one most represented in the membership of that electrophysiology cluster. When the clusters are dissimilar, this rule can result in multiple electrophysiology clusters "matching" the same morphology cluster, which leaves some morphology cluster(s) without a corresponding electrophysiology cluster (Fig. 2*F*).

Analysis of visual receptive field properties. Although spontaneous firing was rare or absent in the vast majority of cells (median spontaneous firing rate was 0.03 spikes/s), 6% of cells had spontaneous firing rates between 1 and 4 spikes/s, and we subtracted the average baseline firing for each cell from all visual responses. Spatial receptive fields were mapped by measuring responses to 500 ms flashes of 2.5, 5, or 10° squares of light (depending on the size preference of the cell) presented at different positions. To calculate spatial receptive field size, we linearly interpolated the "on" response (spikes during the stimulus) and "off" response (spikes during the first 500 ms after stimulus offset) maps in azimuth and elevation to 1° resolution and calculated the number of 1° boxes that exceeded half of the maximum on or off response, respectively. Some cells responded poorly or not at all to stationary flashes of any size but robustly responded to small moving spots. In these cells, we mapped the spatial receptive field by presenting upward and downward moving spots at varying azimuth and leftward and rightward moving spots at varying elevation (responses to upward and downward movement were averaged, as were responses to leftward and rightward movement). A two-dimensional response map was constructed by taking the square root of the product of the responses for each azimuth–elevation combination. Spatial receptive field size was then calculated as described above. When possible, the center of the spatial receptive field (necessary for subsequent stimuli) was determined during the recording by fitting the spatial response map to a two-dimensional Gaussian function; if this fit failed, the center of the receptive field was chosen by eye.

Size tuning curves were generated by measuring spike-count responses to stationary spots of light (500 ms flash) presented at the center of the spatial receptive field or to spots that moved through the receptive field center (the latter were used when responses to the former were weak or absent). Spot diameters were 0.5, 1, 2, 4, 8, 16, and 32° (sometimes additional sizes were presented). Size tuning curves were fit to a gamma function (Nover et al., 2005) because of its flexibility to capture a wide variety of tuning curve shapes (e.g., those of cells that prefer the smallest, largest, or intermediate size stimuli):

$$R(s) = R_0 + A\left(\frac{(\alpha(s-\tau))^n \times \exp(-\alpha(s-\tau))}{n^n \times \exp(-n)}\right),$$

where $R(s)$ is the mean response as a function of stimulus size, R_0 and A are the baseline and maximum responses, respectively, and α, τ, and n determine the shape of the tuning curve. The preferred/best size was determined from the peak of the size-tuning fit, and the size tuning width was defined as the range of sizes over which the response of the cell was greater than half of the maximum response.

Responses to spots of preferred size moving in eight, equally spaced directions at 30°/s were used to calculate a direction-selectivity index (DSI) as the vector sum of responses normalized by the scalar sum of responses (such that the index varies between 0 and 1). The angle of this vector sum defined the preferred direction of each cell.

Responses to spots of preferred size moving in the preferred direction at different speeds (10, 20, 40, 80, 160, and 320°/s) were used to generate speed tuning curves. Responses were measured as the peak of the mean spike-density function (SDF; see next paragraph) for each speed, and preferred speed and speed tuning width were determined from a gamma-function fit as described above for size tuning. Although speed tuning curves for each cell varied to some degree on the duration of the window used to calculate response magnitude, results were qualitatively similar regardless of the metric used.

For each stimulus size, direction, and speed tested, mean SDFs were calculated with 1 ms resolution by convolving individual-trial spike times with a Gaussian filter of width 20 ms (Baker and Gerstein, 2001) and then averaging across trials. "Movement selectivity" for a series of response-window durations was determined by comparing SDFs for stationary stimuli and stimuli moving through the same location: for each response-window duration, the movement-selectivity index (MSI) is the difference between the maximum response for any moving-stimulus SDF over that window duration and the same for any stationary-stimulus SDF, divided by the sum of these two responses.

Drifting sinusoidal gratings were presented at all combinations of the following spatial and temporal frequencies—0.01, 0.02, 0.04, 0.08, 0.16, 0.32, 0.64 cycles/° and 0.25, 0.5, 1, 2, 4, 8, 15 cycles/s—and in at least two directions/orientations (one with horizontally oriented bars and the other with vertically oriented bars). The mean response as a function of spatial and temporal frequency was fit with a two-dimensional Gaussian function in which the preferred temporal frequency could depend on the spatial frequency of the stimulus (Priebe et al., 2003, 2006; Andermann et al., 2011):

$$R(\mathrm{sf},\mathrm{tf}) = A \times \exp\left(\frac{-(\log_2\mathrm{sf} - \log_2\mathrm{sf}_0)^2}{2\sigma_{\mathrm{sf}}^2}\right) \times \exp\left(\frac{-(\log_2\mathrm{tf} - \log_2\mathrm{tf}_p(\mathrm{sf}))^2}{2\sigma_{\mathrm{tf}}^2}\right),$$

where $R(sf,tf)$ is the mean response for each combination of spatial and temporal frequency, A is the maximum response of the neuron, sf_0 is the preferred spatial frequency, tf_0 is the preferred temporal frequency over all spatial frequencies, and $tf_p(sf)$ is the preferred temporal frequency at a particular spatial frequency. The relationship between the preferred temporal frequency and stimulus spatial frequency can be described as follows:

$$\log_2 tf_p(sf) = \xi(\log_2 sf - \log_2 sf_0) + \log_2 tf_0$$

or

$$tf_p(sf) = \left(\frac{sf}{sf_0}\right)^{\xi} \times tf_0,$$

where ξ is the linear relationship of the preferred temporal frequency and stimulus spatial frequency in log spatial-frequency space or the exponent describing the power law relationship between preferred temporal frequency and stimulus spatial frequency in linear spatial-frequency space. When $\xi = 0$, there is no relationship between the preferred temporal frequency and the stimulus spatial frequency. When the preferred temporal frequency is proportional to the stimulus spatial frequency ($\xi = 1$), responses are strongest for a constant speed, and the neuron is said to be "speed tuned"; hence we refer to ξ as the "speed tuning index."

In some cells, gratings were presented in eight, equally spaced directions/orientations. Direction selectivity was calculated as described above (DSI). Preference for motion along a particular axis with the same grating orientation was calculated as follows: 1 − circular variance (Ringach et al., 2002); we refer to this metric as the orientation-selectivity index (OSI). The OSI is conceptually similar to the DSI. Responses for each axis (comprising two, opposing directions) are summed and represented by a single direction with equal spacing; 1 − circular variance is then equivalent to the vector sum divided by the scalar sum of responses in this space.

Statistics. We used the Kruskal–Wallis test, followed by Wilcoxon's rank-sum tests to test whether parameter values (such as DSI) showed a significant tendency to be larger for one cell type versus another. With four cell types, there are six possible comparisons; significance was defined as $p < 0.05/6$ (Bonferroni's correction). These statistical tests were also used to compare responses for the experiments shown in Figures 3*C* and 4*D*. For the data shown in Figure 3*C*, we compared responses to one spot (moving through the center of the receptive field) with responses to two spots (one of which was spatially offset from the receptive field center at one of four locations); significance was $p < 0.05/4$. For the data shown in Figure 4*D*, we compared responses to the sequential or random-with-motion stimulus with responses to the random stimulus for each bin size (a total of seven comparisons); significance was $p < 0.05/7$.

To analyze the distribution of preferred directions of directionally selective neurons (defined as those with DSI > 0.25), preferred directions were binned into quadrants corresponding to the four cardinal directions (up, down, right, and left). χ^2 tests were used, for each of the four cell types, to determine whether the distribution of preferred directions deviated significantly from equal numbers of cells preferring each direction. Significance was $p < 0.05/4$.

Results

Morphological and electrophysiological characteristics independently distinguish the same four sSC cell types

Neurons in the sSC have traditionally been classified on the basis of qualitative morphological criteria (Langer and Lund, 1974). Here we sought to classify sSC neurons via quantitative morphological characteristics and to validate these classes by independently classifying the same cells on the basis of other cellular properties (e.g., electrophysiology).

Neuronal morphology was visualized by filling cells with fluorescent dye during whole-cell recordings performed *in vitro* ($n = 237$) or electroporating the intracellular label Neurobiotin during cell-attached ("loose seal") extracellular recordings performed *in vivo* ($n = 171$; Fig. 1*A*). From images of each cell, we extracted eight morphological parameters, such as dendritic arbor width, primary dendrite thickness, and distance of the soma from the dorsal surface of the SC (see Materials and Methods). The degree to which sSC cells differed was then quantified via hierarchical clustering on the basis of these parameters and visualized via dendrograms (Fig. 1*B*) or principal component analysis (Fig. 1*C*). We found that the separation between the first four clusters of neurons was large relative to the separation between additional clusters for data obtained *in vitro* (Fig. 1*B*, inset) and *in vivo*, suggesting the presence of four sSC cell classes. Probability distributions of several morphological parameters that contributed to distinguishing neurons in these putative four cell classes are shown in Figure 1*D*.

We chose to use existing nomenclature to describe the four classes of sSC cells (see Discussion). Like wide-field (WF) cells, neurons in cluster 1 have somas in the deepest portion of the sSC (the optic fiber layer) and extend thin, elaborately branched dendrites obliquely to the dorsal surface of the sSC. Like horizontal cells, neurons in cluster 2 have long, horizontally extending dendrites with relatively sparse branching. Like narrow-field (NF) cells, neurons in cluster 3 have thick primary dendrites that extend ventrally (into the optic fiber layer) and dorsally to the sSC surface. Like stellate cells, neurons in cluster 4 have a limited field of thin dendrites extending in several directions.

Can neurons distinguished morphologically be distinguished by other characteristics as well? Is four the appropriate number of sSC neuron classes? We, like others (Ascoli et al., 2008), reasoned that the presence and number of distinct neuronal classes is best validated when independent sets of parameters cluster cells into the same groups. Thus, we clustered the same cells on the basis of morphological (Fig. 1) or electrophysiological (Fig. 2) characteristics assayed *in vitro*. In both datasets, the separation between the first four clusters was large relative to the separation between additional clusters (Figs. 1*B*, inset, 2*B*, inset). The similarity between the clusters based on morphological or electrophysiological properties (see next paragraph) allowed us to use the same nomenclature to describe the cells in both sets of clusters: WF cells had relatively depolarized resting potentials and, as noted previously (Endo et al., 2008), the largest and fastest depolarizing sag in response to hyperpolarizing current injection, horizontal cells had high input resistance and were the only cells that could not sustain firing rates above ~100 spikes/s, NF cells had the most hyperpolarized resting potential and low input resistance, and stellate cells exhibited a long ADP after depolarizing current injection.

Quantitative comparison of clusters based on morphological or electrophysiological parameters revealed that cells were most similarly classified when the number of clusters was four (see Materials and Methods; Fig. 2*E*). Moreover, four was the only number for which each morphology cluster had one and only one corresponding electrophysiology cluster (Fig. 2*F*). Overall, the probability that a cell was grouped into the same class on the basis of morphological and electrophysiological criteria was 92%; thus, cell types defined by morphological parameters predicted cell types defined by electrophysiological parameters and vice versa (Fig. 2*F*, inset). These results and the identification of transgenic mouse lines exhibiting cell type-specific expression of Cre recombinase (see last section of Results and Fig. 7) strongly imply the presence of at least four distinct, readily identifiable cell types in the sSC.

Distinct sSC cell types respond to distinct characteristics of visual stimuli

Morphological and intrinsic electrophysiological properties independently define four consistent cell types in the sSC. Do these classes of neurons respond to distinct characteristics of visual stimuli, or are the features of stimuli to which a given sSC neuron responds uncorrelated with its morphological and biophysical characteristics? To distinguish between these possibilities, we characterized stimulus-evoked activity of sSC neurons via loose-seal, cell-attached recordings in urethane-anesthetized mice; electroporation of Neurobiotin at the end of each recording enabled subsequent morphological identification of the cell ($n = 171$).

Visual input to the sSC, like most other areas of the visual system, is organized retinotopically (Dräger and Hubel, 1975; O'Leary and McLaughlin, 2005). Hence, cell types with larger dendritic fields can sample input from a larger area of visual space and may, therefore, exhibit larger receptive fields. To test this possibility. we compared the range of stimulus locations that elicited activity in the different classes of sSC neurons. We found that WF and horizontal cells, which have the largest dendritic arbors (Fig. 1D_1), were responsive to stimuli presented over a significantly broader area of space than NF or stellate cells ($p < 10^{-8}$; Fig. 3*A*).

Cells with large dendritic arbors and receptive fields do not necessarily respond best to large stimuli. Indeed, WF cells exhibited the broad receptive fields, but 70% of the population responded best to stimuli <2° in diameter (Fig. 3*A*,*B*); that is, WF cells responded to small stimuli presented anywhere within a large region of space. Conversely, the preferred stimulus size of horizontal cells was significantly larger than that of WF cells and the cell types with smaller receptive field areas (NF and stellate; $p < 10^{-3}$).

The observation that most WF cells respond best to stimuli occupying a tiny fraction of their spatial receptive field and are inhibited by slight increases in stimulus size suggests that stimuli at any position in the receptive field can recruit local surround inhibition. How does spatial summation operate over broader spatial scales in WF (and other) cells? For example, does a second small stimulus moving through or outside of the excitatory receptive field influence response magnitude? We found that WF cells almost always responded more strongly to a single spot moving through the center of the receptive field than to the same stimulus

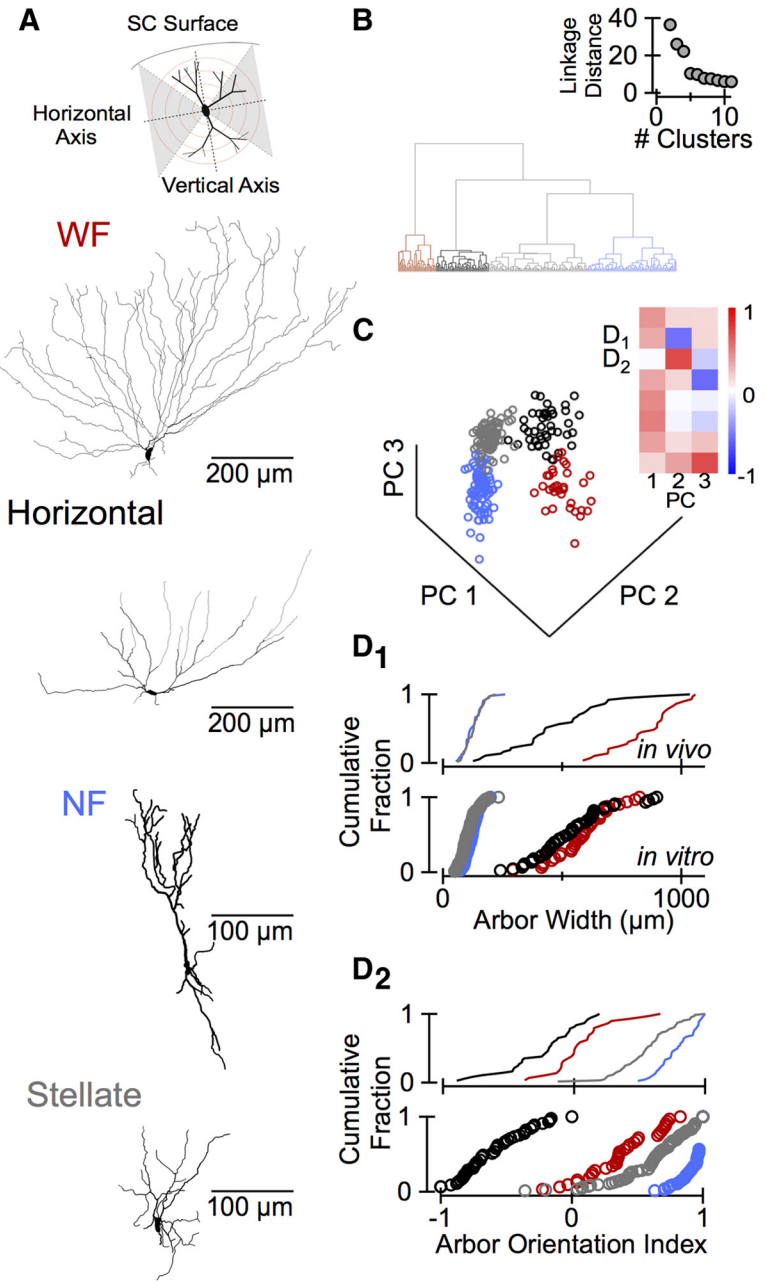

Figure 1. Identification of four sSC cell types on the basis of their somatodendritic morphology. ***A***, Top, Schematic illustrating how morphological parameters were determined. The distance of the soma from the SC surface was measured along the vertical axis, and dendritic arbor width was measured along the horizontal axis. Red dashed circles are Sholl radii used to measure dendritic branching patterns. Gray shaded quadrants between dashed gray lines are "horizontal quadrants," and the nonshaded quadrants are "vertical quadrants" used to calculate the dendritic arbor orientation index. For additional details, see Materials and Methods. Below the schematic are tracings of example neurons from each of four classes. ***B***, Dendrogram representing, via vertical line lengths, the separation (linkage distance) in morphological parameter space of cells filled *in vitro*. Vertical line ends at the bottom on the dendrogram represent individual cells ($n = 237$). Horizontal lines join similar cells into clusters. The four clusters shown in different colors correspond to the four cell classes described in this study. Inset, Linkage distance between the two least-separated clusters as the total number of clusters increases. For example, the first point is the distance between the first (red cells) and second (all other cells) clusters if the total number of clusters is two, the next point is the distance between the second (black cells) and third (gray plus blue cells) clusters if the total number of clusters is three, and so on. ***C***, All cells plotted in morphological parameter space with cell class denoted by color. The three axes (principal components) correspond to the linear parameter weightings that maximize the spread of the entire population of cells. Parameter weightings are shown in the plot to the right, in which each row is a parameter (in the same order as described in Materials and Methods starting from the top) and each column is a principal component. The parameters shown in D_1 and D_2 are indicated. Dark red or blue indicates a strong contribution of a parameter to the variance along an axis. The first three principal components accounted for 45, 22, and 14% of the total variance, respectively. ***D***, Cumulative probability distributions of the dendritic arbor width (***D***$_1$) and dendritic arbor orientation index (***D***$_2$) for cells of each class recorded *in vivo* (lines) or *in vitro* (circles). Differences between *in vitro* and *in vivo* datasets likely reflect that cells were filled and imaged in live 400 μm sections (*in vitro*) or filled in intact brains but imaged in fixed tissue (*in vivo*).

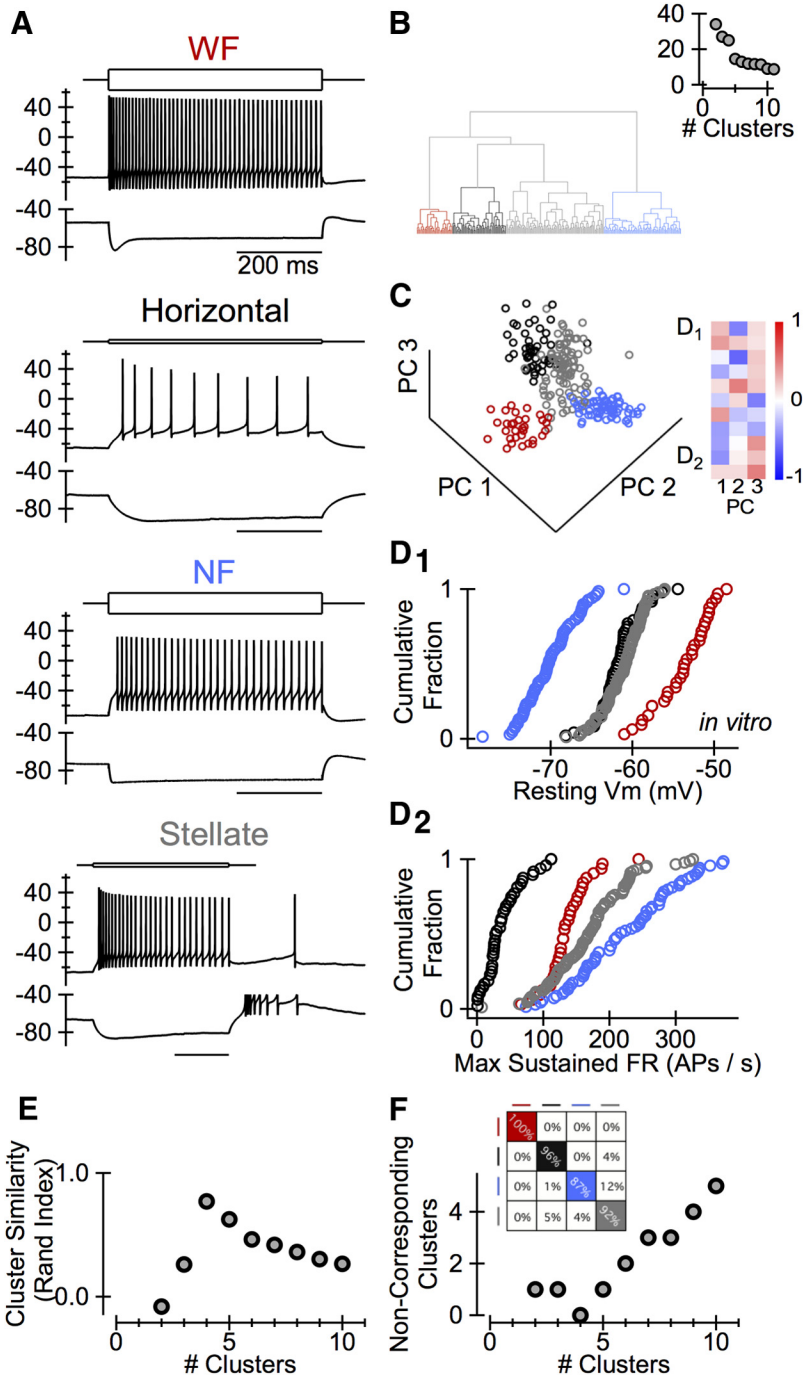

Figure 2. Electrophysiological and morphological properties independently identify four nearly identical cell classes. ***A***, Responses to current injection in example neurons from each of four classes. Straight black lines above each trace indicate current amplitude and duration. Current steps were 500 ms and ±600 pA for the WF and NF cell examples and ±100 pA for the horizontal and stellate cell examples. The data displayed after the current step are extended for the stellate cell example to show the prolonged ADP after positive current injection or rebound potential after negative current injection; rebound spikes after negative current injection are truncated. ***B***, Dendrogram representing the separation of all recorded cells ($n = 237$) in electrophysiological parameter space and linkage distance between the two least-separated clusters as the total number of clusters increases. ***C***, All cells plotted in electrophysiological parameter space with cell class denoted by color. As in Figure 1*C*, the plot to the right shows the contribution of each parameter to the variance along each axis (for list of parameters, see Materials and Methods). The first three principal components (PC) accounted for 35, 19, and 16%, respectively, of the variance across all cells. ***D***, Cumulative probability distributions of the resting potential (***D*$_1$**) and maximum sustained firing rate (FR; ***D*$_2$**). ***E***, Similarity (Rand index; see Materials and Methods) between clusters based on morphological or electrophysiological properties as a function of the total number of clusters. ***F***, Number of morphologically defined clusters lacking a corresponding electrophysiologically defined cluster (see Materials and Methods) as a function of the total number of clusters. The inset shows how cells belonging to the four clusters based on morphological parameters (rows) are classified into corresponding clusters on the basis of electrophysiological parameters (columns). The value in the second row, fourth column, for example, indicates that 4% of cells classified as horizontal cells on the basis or morphological properties were classified as stellate cells on the basis of electrophysiological properties. Positions along the diagonal (colored boxes) show the percentage of cells classified into the same class (92% overall). Some rows do not sum to 100% because of rounding. Some columns do not sum to 100% because the number of cells in corresponding morphological or electrophysiological clusters can differ.

accompanied by a second, spatially offset, spot moving in parallel (Fig. 3*C*). The suppressive effect of the second spot increased in strength as its distance from the first spot (and thus from the center of the receptive field) increased. This result is consistent with a wider-acting suppressive mechanism through which even small stimuli, especially near the receptive field edge, can strongly suppress responses to other objects. Similarly wide-acting suppression was observed in NF cells despite the much smaller excitatory receptive fields of these cells. In contrast, a second moving spot facilitated or had no effect on the response of horizontal and stellate cells to the primary spot (Fig. 3*C*).

Another distinguishing feature of WF cells is that they responded weakly to stationary stimuli relative to moving stimuli (Fig. 4*A*). To quantify this difference, we compared the best response of each cell to a stationary and moving spot (Fig. 4*B*,*C*$_1$; see Materials and Methods). WF cells were the only cell type that strongly preferred moving stimuli regardless of the temporal window over which response magnitude was calculated ($p < 10^{-5}$; Fig. 4*C*$_2$). Does the apparent "movement selectivity" of WF cells reflect sensitivity to object motion or a more general preference for "dynamic spatiotemporal stimuli" over static stimuli (Luksch et al., 2004)? To answer this question, we compared responses to "sequential" movement of a stimulus, in which a spot of light progressed from one adjacent location to the next, and "random" motion, in which the spot appeared at the same locations but in random order. The number of these locations varied such that the spot traversed the same 30° path over 1 s each trial but the distance between, time spent occupying, and order of each location along the path varied (Fig. 4*D*$_1$). WF cells strongly preferred the sequential stimulus as long as the distance between successive locations was small (Fig. 4*D*$_2$); that is, WF cells preferred stimuli that indicate continuous motion.

To determine how much motion is required for WF cells to distinguish moving and static stimuli, we compared responses to the random stimulus and a similar

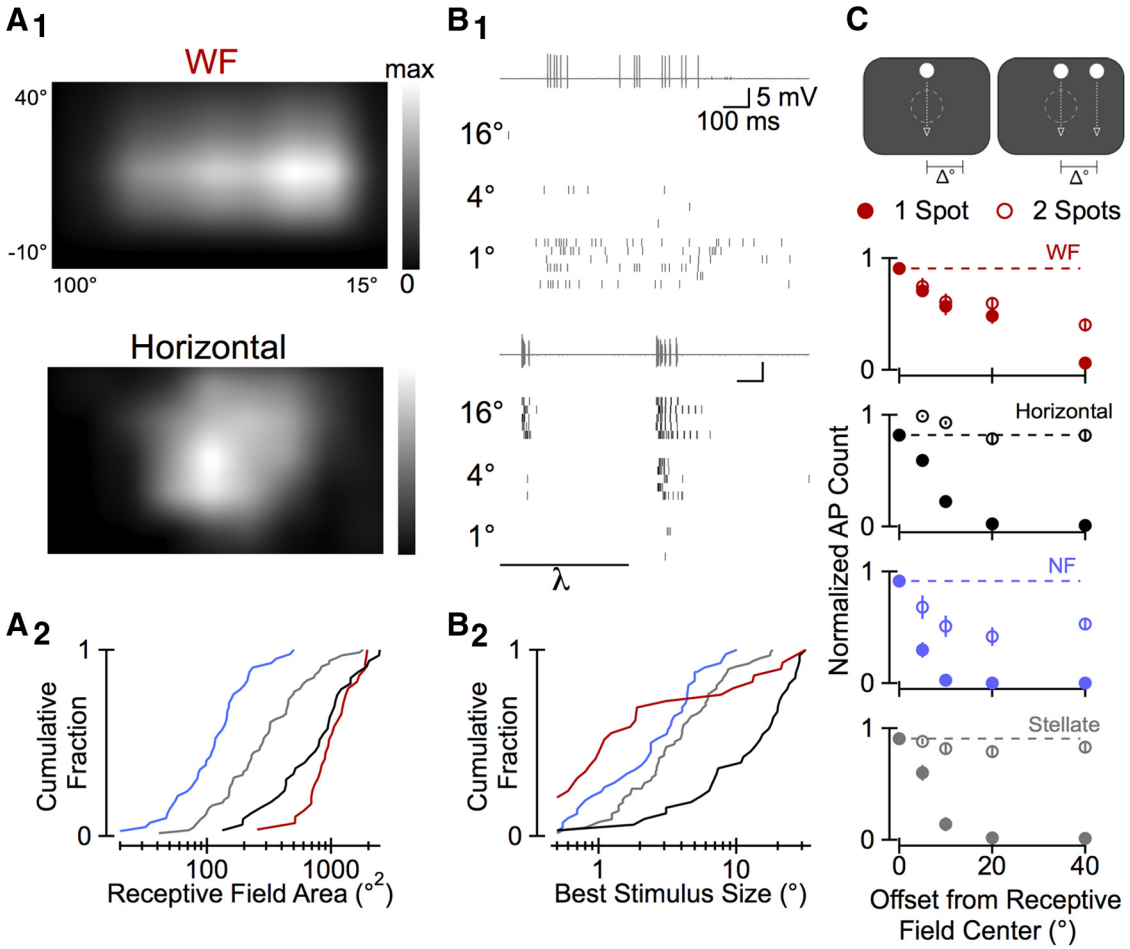

Figure 3. Relationship between spatial receptive field size and optimal stimulus size. ***A*$_1$**, Spatial receptive field map of an example WF and horizontal cells. Lighter regions correspond to regions of space in which the cell responded to visual stimuli. For the horizontal cell, responses to a 10° square spot presented in a grid of positions were normalized to the maximum response and smoothed. For the WF cell, moving spots (1°) were used to map the spatial receptive field (and determine size tuning) because the cell responded poorly to stationary stimuli (see Materials and Methods). ***A*$_2$**, Cumulative probability distributions of the receptive field size of all WF (red), horizontal (black), NF (blue), and stellate (gray) cells recorded. ***B*$_1$**, Responses of cells shown in ***A*** to moving (WF) or stationary (horizontal) spots of varying diameter. At the top are example raw extracellular recording traces, and at the below are raster plots representing spike times for several presentations of three of the spot diameters tested. The line labeled λ indicates the onset and duration of stationary spot presentation for the horizontal cell. ***B*$_2$**, Cumulative probability distribution of the stimulus size that evoked the largest response in all cells. ***C***, Mean responses (normalized to the largest response in each cell) to one (filled symbols) or two (open symbols) small spots (0.5–2°) moving in parallel at various positions relative to the receptive field center. During two-spot trials, one spot moved through the receptive field center and the second spot moved in parallel at one of the positions indicated by open symbols. Responses to two moving spots were significantly less than the response to a single spot moving through the center of the receptive field when the distance between the two spots was ≥10° in WF ($n = 12$) and NF ($n = 9$) cells. In horizontal cells ($n = 8$), responses to two moving spots were significantly greater than the response to a single spot when the two spots were separated by ≤10°. Responses to one or two moving spots did not significantly differ in stellate cells ($n = 13$).

stimulus during which the spot moved locally near each random position ("random with motion"; Fig. 4*D*$_1$). WF cells preferred the stimulus with local motion when the range of movement was as small as 6° (comparable with the size of the receptive fields of many retinal ganglion cells; Sagdullaev and McCall, 2005; Koehler et al., 2011; Fig. 4*D*$_2$). Thus, motion within the receptive field of individual inputs to WF cells, but only small scattered portions of the WF cell receptive field, was sufficient to drive movement-selective responses.

Movement-selective cells do not necessarily prefer a particular direction of motion; likewise, a direction-selective cell is not necessarily movement selective. Therefore, we asked whether direction-selective sSC neurons were restricted to certain sSC cell types or distributed across all four types. Direction selectivity was significantly stronger across the population of WF and NF cells compared with stellate and horizontal cells (Fig. 5*A*,*B*). Previous studies of (unidentified) mouse sSC cells also described directionally selective neurons but differed in whether the preferred directions of these cells were uniformly distributed (Wang et al., 2010) or strongly biased for upward motion (Dräger and Hubel, 1975). We found that the preferred directions of directionally selective WF cells (those with DSI > 0.25), but not the other cell types, deviated significantly from equal distribution into the four cardinal directions ($p < 0.01$; Fig. 5*C*); seven of nine directionally selective WF cells preferred upward motion (i.e., the angle of the vector sum of their responses was within 45° of straight up).

The response of sSC neurons to moving spots also depended strongly on stimulus speed. The stimulus speed that elicited the most activity in horizontal cells was significantly faster than the preferred speed of the other cell types regardless of the window duration used to calculate response magnitude ($p < 10^{-3}$; Fig. 5*D*).

Many studies of the visual system in mice (and other mammals) use drifting sinusoidal gratings rather than spots. Full-field gratings (50° × 50° or larger), in particular, are common because this stimulus allows simultaneous characterization of multiple

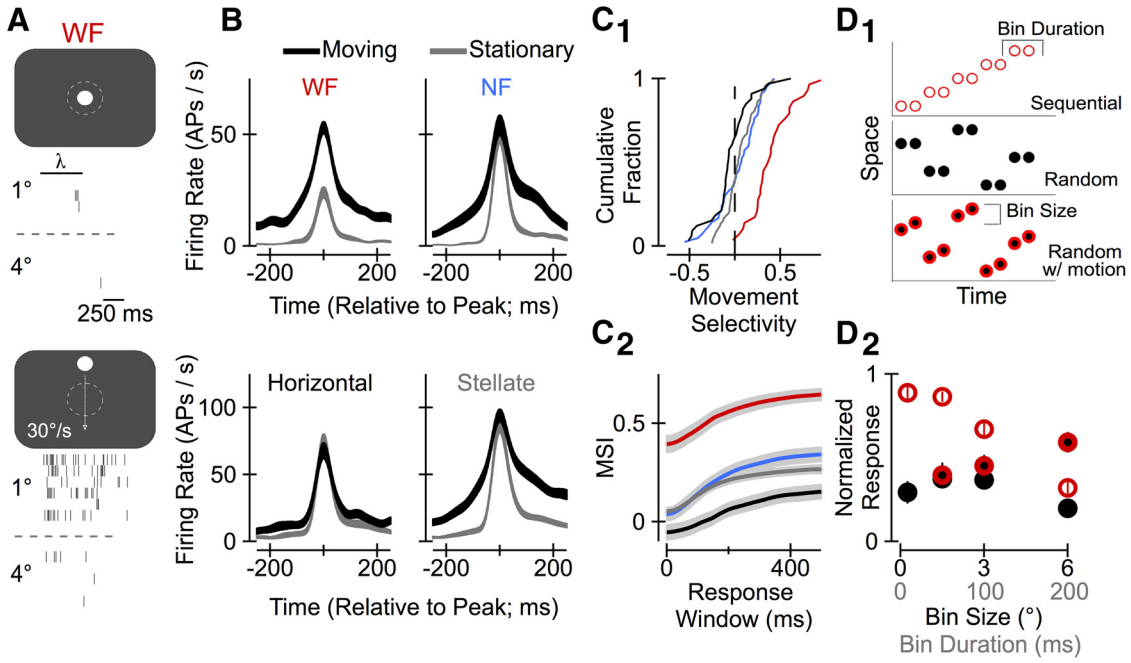

Figure 4. Comparison of responses to stationary and moving stimuli. ***A***, Raster plots from an example WF cell showing the number and timing of spikes in response to several presentations of a stationary spot (1 or 4° diameter) presented at the center of the receptive field or an identical spot moving through the same location. The line labeled λ indicates the onset and duration of stationary spot presentation. ***B***, Peak-aligned, mean SDFs for responses to the stationary and moving stimuli that elicited the largest response in all WF, horizontal, NF, and stellate cells. Line thickness corresponds to SEM. C_1, Cumulative probability distribution of the MSI (see Materials and Methods) for peak responses in all cells recorded. MSI values above 0 indicate a preference for moving stimuli. C_2, Relationship between the MSI (mean ± SEM) and the duration of the window used to calculate response magnitude. D_1, Schematic describing an experiment in which a small spot (0.5–2°) moved sequentially (open red circles) along a straight line (30° at 30°/s) or appeared at the same positions along this line in random order (filled black circles). The circles represent the position of the spot at a each frame (120 frames/s). The spot was stationary for a variable duration (1–24 frames) at spatially "binned" positions or moved locally through each (randomly ordered) bin (filled black circles with red stroke). D_2, Mean responses (normalized the maximum response of each cell) of 14 WF cells to the stimuli described in the schematic. Responses to the sequential stimulus (open red circles) were significantly larger than those to the random stimulus (filled black circles) for bin sizes ≤3°. Responses to the random stimulus with local motion (filled black circles with red) were significantly greater than responses to the random stimulus for the 6° bin.

cells with different receptive field locations. How do sSC neurons respond to such stimuli? Presentation of gratings that varied in size, spatial/temporal frequency, or orientation to a subset of cells allowed us to make several additional observations that complemented our findings with spot stimuli. We found that nearly all horizontal (20 of 20) and stellate (27 of 29) cells, but only a small fraction of WF (5 of 15) and NF (4 of 19) cells, responded to full-field (80° × 50°) stimulation. Gratings occupying smaller areas (20° × 20° or 10° × 10°) triggered activity in all of the NF cells and most (7 of 10) of the WF cells that did not respond to full-field stimulation. This result, like responses to two moving spots (Fig. 3*C*), suggests that WF and NF cells are subject to more powerful surround suppression than stellate and horizontal cells.

The spatial frequency of gratings influenced response magnitude in a manner that was similar to spot diameter: horizontal cells, which responded strongly to large spots, preferred gratings with significantly lower spatial frequencies than the cell types that responded best to smaller spots (WF, NF, and stellate cells; $p < 0.01$; Fig. 6*A*,*B*). WF, NF, and stellate cells were also similar to each other but differed from horizontal cells in that their preferred temporal frequency increased as the spatial frequency increased (Fig. 6*A*,*C*); these cells thus prefer a constant speed rather than a particular temporal frequency. Similarly "speed tuned" cells have been observed in primate and mouse visual cortex but not the retina (Priebe et al., 2006; Andermann et al., 2011). We also encountered some cells in sSC that, like cells in V1, responded preferentially to motion in either direction along an oriented axis. We found examples of neurons from all four cell types that were orientation but not direction selective; orientation selectivity was not substantially stronger or more common in any particular cell type (Fig. 6*D*).

Anatomical targets of the sSC receive input from different subsets of sSC cell types, including GABAergic cells

The results presented above indicate that distinct classes of sSC neurons respond to distinct features of visual stimuli. To what extent do these classes of neurons convey information to distinct downstream nuclei? We used two techniques to answer this question. First, we identified transgenic mouse lines in which Cre recombinase is expressed in specific sSC neurons and used Cre-dependent expression of fluorescent proteins to visualize the axonal projections of these cells. Second, we identified the sSC cell types retrogradely labeled from putative downstream targets. These targets include the PBg (a brainstem nucleus that provides cholinergic feedback to the sSC), LP (part of the pulvinar), vLGN (also referred to as the perigeniculate nucleus), and dLGN.

To identify transgenic mice in which Cre recombinase was expressed in one but not the other three neuronal classes, we injected virus coding for Cre-dependent expression of green fluorescent protein (GFP) or a ChR2–GFP fusion protein into the sSC. Subsequent *in vitro* recordings and cluster analysis were used to classify labeled and unlabeled cells from these mice.

We first determined the identity of sSC neurons that produce and package into vesicles the neurotransmitter GABA. A previous study using GABA immunolabeling and qualitative identification of sSC cells (based on somatic and proximal dendrite mor-

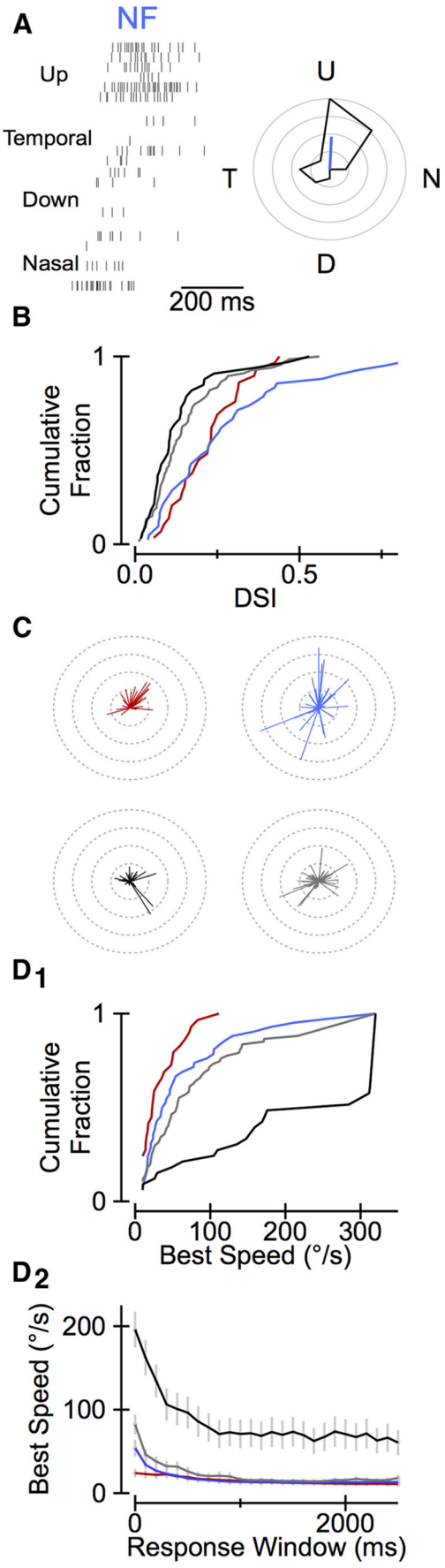

phology) suggested that both stellate and horizontal cells might be GABAergic (Mize, 1988). In a more recent study, all of the labeled cells in Gad1–GFP mice were identified as horizontal cells (Endo et al., 2003); Gad1 is an isoform of the gene encoding the enzyme responsible for GABA biosynthesis. Consistent with the latter study, we found that horizontal cells were the only cell type labeled after virus injections in mice in which Cre is expressed under the control of the promoter for Gad2 (the other Gad isoform; Fig. 7). Moreover, horizontal cells were also the only cell type labeled in Gad2–Cre mice crossed with mice (Ai9) in which TdTomato expression is Cre dependent (11 of 11 horizontal, 0 of 10 stellate, 0 of 6 WF, and 0 of 6 NF cells) and, with one exception, the only cells labeled in vGAT–ChR2–GFP knock-in mice (11 of 11 horizontal, 1 of 10 stellate, 0 of 6 WF, and 0 of 5 NF cells). The observation that ~70% of horizontal cells were labeled in virus-injected mice (Fig. 7*C*), whereas all horizontal cells were labeled in the Gad2–Cre × Ai9 cross and vesicular GABA transporter (vGAT) knock-in mice, suggests the virus did not infect every Cre-expressing cell. Together, these results indicate that horizontal cells are likely the only GABAergic cell type in the sSC.

Searching the GENSAT database (Gerfen et al., 2013) revealed at least two potential bacterial artificial chromosome transgenic mice in which Cre appeared to be expressed in a subset of sSC neurons. Indeed, only WF cells were labeled in sSC slices from Ntsr1–GN209–Cre mice, and only NF cells were labeled in the sSC of Grp–KH288-Cre mice (Fig. 7).

Cell-type specific, Cre-dependent expression of fluorescent proteins or light-gated ion channels enables the identification and manipulation of the downstream regions to which specific subsets of sSC cells project. For example, selective labeling of horizontal cells in the sSC of Gad2–Cre mice revealed axon terminals in several nuclei, including the PBg, the dorsolateral portion of dLGN, and the vLGN (Fig. 8A_1). To confirm these putative inhibitory synaptic contacts, we injected virus coding for conditional ChR2 expression in the sSC of Gad2–Cre mice and recorded postsynaptic potentials elicited by activation of ChR2-expressing axons in regions downstream of the sSC (Fig. 8A_2). We observed IPSPs in response to ChR2 stimulation in all PBg (n = 3), vLGN (n = 2), and dLGN (n = 4) cells examined. Responses persisted in the presence of the ionotropic glutamate receptor antagonists NBQX and AP-5 and were abolished by the $GABA_A$ receptor antagonist gabazine. Together, these data strongly suggest that horizontal cells in the sSC provide inhibitory input to the PBg and LGN.

WF and NF cells exhibited more selective projections. The axons of WF cells, labeled in Ntsr1–GN209–Cre mice, densely innervated LP but avoided dLGN and vLGN (Fig. 8B_1). The projection to LP was bilateral: the axons of WF cells continued lateral of LP in the optic tract (dorsal and then lateral of LGN), crossed

←

Figure 5. Direction selectivity and speed tuning of sSC neurons. ***A***, Left, Example raster plots showing responses of an NF cell to a spot moving across the screen in different directions through the receptive field of the cell. Right, Polar plot showing the mean response of this cell to stimuli moving in eight equally spaced directions and the normalized vector sum of these responses (blue line). ***B***, Cumulative probability distributions of the DSI (the normalized vector sum length, as shown in ***A***) for all cells recorded. ***C***, Normalized vector sum for all cells recorded showing the strength of directional preference (vector length) and distribution of preferred directions (vector angles). D_1, Cumulative probability distributions of the speed of a moving spot that evoked the greatest peak response in each cell. D_2, Preferred speed as a function of the window duration used to calculate response magnitude (mean ± SEM). D, Dorsal; N, nasal; T, temporal; U, up.

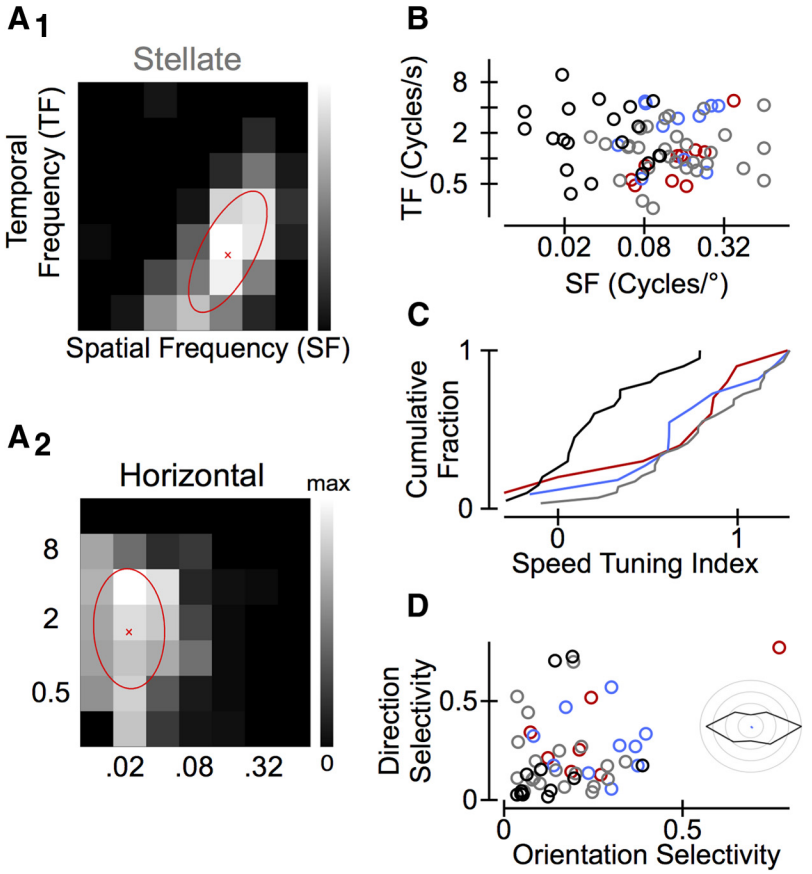

Figure 6. Spatiotemporal frequency tuning and orientation selectivity of responses to drifting gratings. ***A***, Mean responses of example stellate (***A1***) and horizontal (***A2***) cells to gratings with varying combinations of spatial and temporal frequency. Responses were fit to two-dimensional Gaussian function; the mean of this fit is indicated with an × and SD about the mean with a red ellipse. Rightward diagonals in spatiotemporal frequency space follow constant speeds; the Gaussian fit function quantified the dependence of temporal frequency (TF) tuning on spatial frequency (SF), resulting in the "speed tuning index" shown in ***C*** (see Materials and Methods). The speed tuning index was 0.93 for the example stellate cell and −0.09 for the example horizontal cell. ***B***, Mean spatial and temporal frequency of the Gaussian fit to responses in each cell tested. ***C***, Cumulative probability distribution of the speed tuning index for the cells shown in ***B***. ***D***, Scatter plot of the orientation selectivity and direction selectivity of all cells tested. The inset shows mean responses to gratings moving in eight equally spaced directions for an example NF cell. This cell is orientation selective (OSI = 0.3) but not direction selective (DSI = 0.06).

the optic chiasm, and followed the optic tract into the contralateral LP. Virus injections in the sSC of Ntsr1–GN209–Cre mice retrogradely labeled PBg neurons (Fig. 8B_1), making it difficult to determine whether WF cells project to this region. NF cells, labeled in Grp–KH288–Cre mice, ramified in the intermediate gray layer of the SC (directly under the optic fiber layer) and the PBg (Fig. 8C_1). The axons of NF cells also followed the optic tract dorsal of LP but did not ramify ventrally into LP or continue laterally to LGN (Fig. 8C_1). Activation of ChR2 expressed in WF or NF cells triggered monosynaptic glutamatergic EPSPs in their respective downstream targets (Fig. 8B_2,C_2), i.e., postsynaptic potentials that could be evoked in the absence of APs when axon terminals were depolarized (Petreanu et al., 2009) and were blocked by NBQX and AP-5 (WF, $n = 6$ of 6 LP neurons in Ntsr1–GN209–Cre mice; NF, $n = 5$ of 10 intermediate layer SC neurons and 4 of 4 PBg neurons in Grp–KH288–Cre mice). Thus, WF and NF cells provide excitatory input to a substantial fraction of neurons in the regions they target.

To complement anterograde tracing of WF, horizontal, and NF cells and to identify the areas to which stellate cells project, we recorded retrogradely labeled cells *in vitro* after injections of fluorophore-conjugated beads or cholera toxin into the PBg, LP, or LGN. Injections of cholera toxin or beads into the PBg retrogradely labeled NF (9 of 11) and stellate (5 of 20) cells but not WF (0 of 17) or horizontal (0 of 17) cells. Injections of beads into LP, dLGN, or vLGN retrogradely labeled WF (24 of 29) and stellate (13 of 34) cells (Fig. 8*D*) but not NF (0 of 21) or horizontal (0 of 39) cells. We were not surprised to see similar results across the thalamic regions injected given that axons follow the optic tract dorsal of LP before they reach dLGN and dorsal and lateral of dLGN before they reach vLGN (or, in the case of WF cells, continue to the contralateral hemisphere). Our results are consistent with previous work suggesting that the sSC projections to LP and dLGN originate predominantly from WF and stellate cells, respectively (Mooney et al., 1988).

However, it was unexpected that we did not observe retrogradely labeled horizontal cells from bead or cholera toxin injections into PBg or LGN. One possibility is that horizontal cells internalize and/or transport beads and cholera toxin inefficiently. We took advantage of the fact that adenovirus injections retrogradely label neurons (Harris et al., 2012; Wang et al., 2014) and injected virus coding for Cre-dependent expression of GFP into the PBg or LGN of Gad2–Cre mice. All of the retrogradely labeled cells we recorded in the sSC of these mice were horizontal cells (Fig. 8*E*; $n = 5$, PBg; $n = 5$, LGN). This result, together with anterograde labeling in Gad2–Cre mice, confirms that horizontal cells project to the PBg and LGN.

Discussion

Our results delineate four cell types in the mouse sSC, the distinct features of visual stimuli to which they respond, and the specific and shared downstream regions to which they project (Fig. 9). Moreover, we identified transgenic mouse lines that enable selective manipulation of three of these four cell types. In summary, (1) WF cells respond well to small moving stimuli anywhere within a large region of space and project to LP, (2) horizontal cells are GABAergic neurons that have large receptive fields, respond to large stationary or swiftly moving stimuli, and project to dorsal and ventral LGN and PBg, (3) NF cells have small spatial receptive fields, prefer small stimuli, are often direction selective, and project to the PBg and deeper layers of the SC, and (4) stellate cells, like NF cells, have small receptive fields, prefer small stimuli, and project to the PBg but, unlike NF cells, also project to LGN.

These findings are important for (at least) two reasons. First, the ability to identify neurons, both *in vitro* and *in vivo*, that respond to similar features of visual stimuli enables more detailed insight into the network, synaptic, and biophysical features that shape response selectivity (Briggman et al., 2011; Ko et al., 2011). Second, knowledge of the information that the sSC conveys to different downstream areas, and a means to manipulate the cells

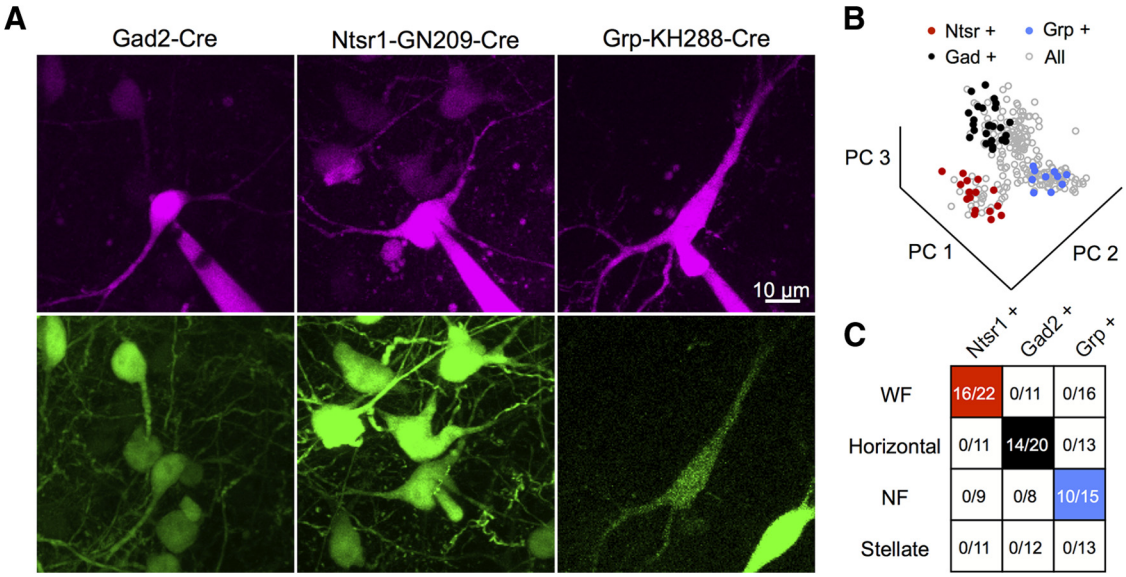

Figure 7. Identification of mouse lines that express Cre recombinase in specific sSC cell types. ***A***, Example horizontal cell recorded in a brain slice from a Gad2–Cre mouse (left), a WF cell from an Ntsr1–GN209 –Cre mouse (center), and an NF cell from a Grp–KH288 –Cre mouse (right). Magenta images (top) show recorded cells filled with Alexa Flour 594; corresponding green images (below) show cells with Cre-dependent GFP expression following virus injection in the sSC. Bright GFP-expressing cells are sometimes visible in the magenta channel, but the Alexa Fluor 594 is never visible in the green channel (hence the recording pipette is only visible in the top images). ***B***, All cells (gray symbols) are plotted in electrophysiological parameter space, as in Figure 2C, with cell expressing Cre from one of the three mouse lines shown with colored symbols. PC, Principal component. ***C***, The fraction of recorded cells of each cell type that expressed Cre in the three mouse lines. For example, we recorded from a total of 53 cells in the Ntsr1–GN209 –Cre line; 22 of these cells were WF cells and 16 of the 22 WF cells expressed Cre. Cells were targeted for recording without knowing beforehand whether they expressed GFP or not. The virus did not necessarily infect every Cre-expressing cell.

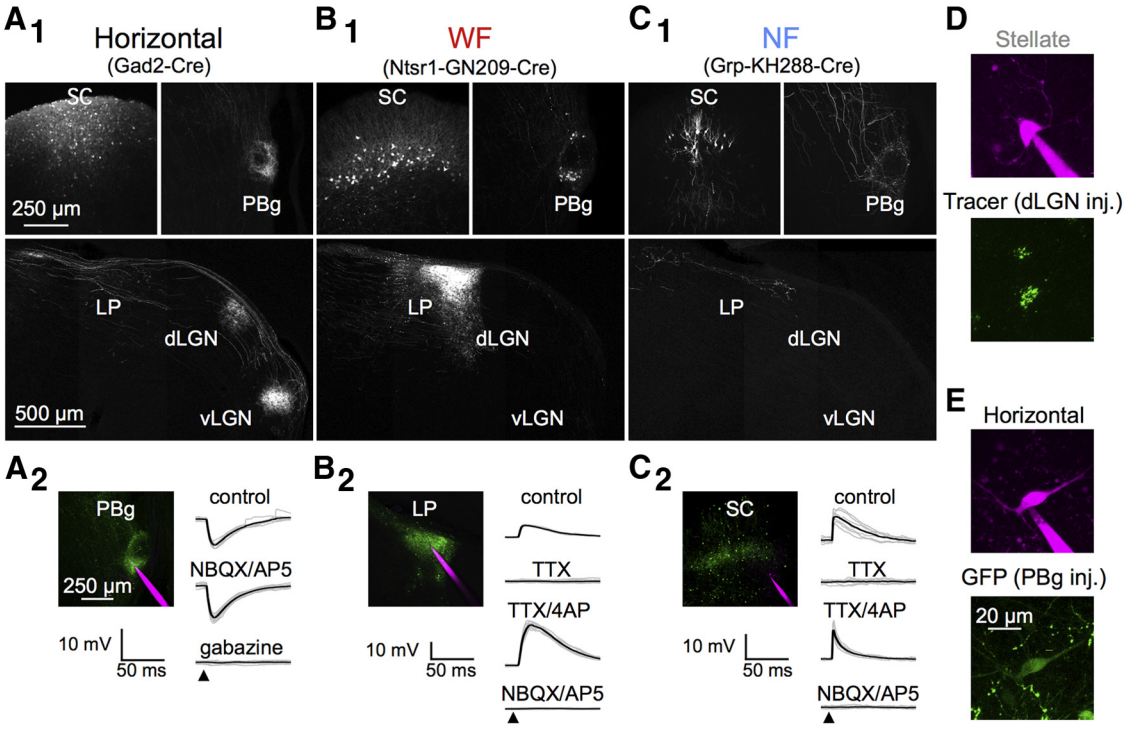

Figure 8. Axonal projections of horizontal (Gad2–Cre), WF (Ntsr1–GN209 –Cre), and NF (Grp–KH288 –Cre) cells. ***A_1***, ***B_1***, ***C_1***, Virus encoding Cre-dependent tdTomato expression was injected into the sSC of mice from each transgenic line. SC images show cell bodies labeled at the injection site and, in the Grp–KH288 –Cre mouse, axons projecting to deeper layers of the SC. Images of the PBg show axon terminals or, in the Ntsr1–GN209 –Cre line, retrogradely labeled somas. The bottom images show, for each Cre line, three different thalamic regions targeted by the sSC. All images show coronal sections; dorsal is up and medial is left. ***A_2***, Recording from a PBg neuron in a slice from a Gad2–Cre mouse in which virus coding for Cre-dependent GFP/ChR2 expression was injected into the sSC. GFP-expressing axons are green, and the recording pipette is magenta. Synaptic responses were evoked by a 1 ms blue light pulse at the time indicated by the black triangle. The baseline membrane potential was −61 mV. ***B_2***, Same as ***A_2*** except the virus injection was in an Ntsr1–GN209 –Cre mouse and the recording was in LP. The baseline potential was −65 mV. ***C_2***, Same as ***A_2*** except the virus injection was in a Grp–KH288 –Cre mouse and the soma of the recorded neuron was in the deep SC and extended its dendrites into the band of GFP-expressing axons in the intermediate SC. The baseline potential was −70 mV. The reduced variability and faster decay kinetics of the EPSP in TTX/4-AP compared with control in this cell may reflect that some ChR2-expressing axon terminals are not severed from their soma, which is unlikely in the PBg (***A_2***) and impossible in the thalamus (***B_2***). ***D***, Example stellate cell that was retrogradely labeled after injection of tracer into the dLGN. ***E***, Example horizontal cell that was retrogradely labeled after PBg injection with virus coding for Cre-dependent GFP expression.

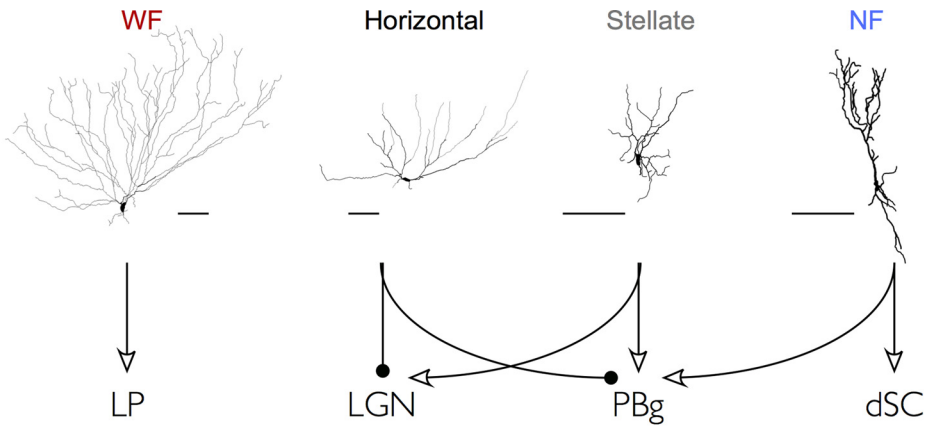

Cre	Ntsr1-GN209	Gad2	--	GRP-KH288
Area	Large	Large	Small	Small
Size	Small	Large	Small	Small
Movement	Yes	No	No	No
Speed	Slow	Fast	Slow	Slow
Direction	Occasional	Rarely	Rarely	Often

Figure 9. Summary of sSC cell types, their projection targets, and the features of visual stimuli to which they best respond. Scale bar, 100 μm. Lines ending in arrowheads or filled circles indicate glutamatergic or GABAergic projections, respectively. Blue/yellow boxes indicate the Cre lines that enable selective labeling/manipulation of particular cell types (top row) or the characteristics of visual stimuli that most effectively trigger activity in each cell type (all other rows). The row labeled Area refers to receptive field size, Size refers to preferred stimulus (spot) size, Movement corresponds to whether a cell prefers moving over stationary spots, Speed refers to preferred speed of moving spots, and Direction indicates how often direction-selective responses were observed in each cell type.

conveying this information are necessary to establish the role of specific sSC cells in downstream visual activity and visually guided behavior.

sSC cell types

Neurons in the sSC, as in many other brain regions, have been classified previously on the basis of qualitative characteristics of their somatodendritic morphology (Langer and Lund, 1974; May, 2006). These studies generally agree on five cell classes in the sSC. In some cases, the electrophysiological properties of these cells were assayed in parallel (Lo et al., 1998; Edwards et al., 2002; Endo et al., 2003), but variability in electrophysiological properties did not strongly correspond to morphological cell classes, and no attempt was made to classify cells independently on the basis of electrophysiological properties. By making this comparison quantitatively, we found a strong correspondence between morphological and electrophysiological characteristics of four classes of sSC neurons. These cells were similarly identified by either morphological or electrophysiological properties alone.

Marginal cells, a fifth putative cell type, have somas at the dorsal surface of the sSC and extend their dendrites ventrally toward the optic fiber layer. Although we filled cells both *in vitro* and *in vivo* that match this description, the electrophysiological properties of these cells were qualitatively similar to those of stellate cells. A simple possibility is that the somas of stellate cells are located throughout the sSC, and those near the dorsal surface extend their dendrites in the only possible direction. Our data do not support splitting stellate cells, or any other cell type, into a coherent fifth type; defining an additional cell type would split either WF cells for the clusters based on morphology or NF cells for the clusters based on electrophysiological properties.

Of course, additional characterization might elucidate further cell type diversity in the sSC based on gene expression, differences in input from the retina and/or visual cortex, or finer distinctions in projection targets. Cell type-selective expression in three Cre lines and the congruence of four (but not less than four) morphologically and electrophysiologically defined clusters make it unlikely that there are fewer than four cell types.

sSC visual response properties

Neurons in the sSC respond to a variety of stimulus characteristics. Many of these characteristics are similar to those of neurons in the retina, dLGN, and V1, e.g., sSC neurons exhibit varying degrees of surround suppression and some prefer a particular stimulus orientation and/or direction of motion (McIlwain and Buser, 1968; Berman and Cynader, 1972; Schiller and Stryker, 1972; Dräger and Hubel, 1975; Wang et al., 2010). Some sSC cells, by comparison, exhibit more unusual properties. A substantial fraction of sSC neurons respond nearly exclusively to stimuli that are small ($<2°$ diameter) and slowly moving anywhere within a large area of visual space; these response properties resemble in several ways those of neurons in insect visual systems (Barnett et al., 2007; Nordström and O'Carroll, 2009).

Contrary to previous results, in which the morphology of small numbers of neurons recorded *in vivo* was evaluated qualitatively (Mooney et al., 1988; Wang et al., 2010), we found that variability in the features of stimuli that triggered activity among sSC neurons correlated with differences in the morphology of neurons generating that activity. For example, nearly all neurons exhibiting movement selectivity also exhibited morphological characteristics of WF neurons. Likewise, the vast majority of cells that responded best to large (>10°) stimuli and lacked speed tuning to gratings had morphological characteristics of horizontal cells. Correspondence between morphology and visual responses has also been seen in X, Y, and W neurons in the dLGN (Friedlander et al., 1979, 1981; Friedlander, 1982). In contrast, cells in V1 that exhibit substantial functional differences, such as simple or complex receptive fields, are nearly equally likely to have pyramidal or stellate morphology (Gilbert and Wiesel, 1979).

A benefit of identifying a relationship between the structure and function of neurons (in the sSC and elsewhere) is that it enables specific, testable hypotheses about how selectivity for size, motion, and/or direction of motion might arise. Many of the stimuli to which WF cells do not respond, for example, drive robust activity in horizontal cells. This relationship, and the fact that horizontal cells are GABAergic, suggests that the receptive field properties of WF cells might be shaped by inhibitory input provided by horizontal cells. Likewise, the observation that strong direction selectivity is primarily restricted to NF neurons suggests that these cells may receive particularly strong input from direction-selective retinal ganglion cells. Hypotheses such as these have been difficult to test in brain regions in which cellular characteristics of the neurons exhibiting particular response properties are unknown.

Distribution of information from the sSC and the role of specific sSC neurons in visually guided behavior

The relationship between morphological and functional properties of sSC neurons also enabled insight into the shared and distinct visual signals that regions downstream of the sSC receive. Our data suggest that each of the three channels through which the sSC can influence visually guided behavior originates from distinct cell types and carries different visual information: (1) horizontal and stellate cells influence the geniculocortical pathway via a projection to dLGN; (2) WF cells project to LP, which connects to several higher-order visual cortical areas; and (3) NF cells provide visual input to deeper layers of the SC involved in orienting movements and spatial attention. Most sSC cell types (other than WF cells) also project to the PBg, a "satellite" cholinergic nucleus that projects back to the sSC and is thought to be involved in stimulus competition for ("bottom-up") attention (Mysore and Knudsen, 2011).

Exactly how specific neurons and/or networks of neurons in the sSC (and elsewhere) subserve visually guided behavior remains a mystery. This gap in understanding does not reflect an absence of appropriate behavioral paradigms or information about the features of stimuli that trigger activity. Rather, until recently, it has been difficult to assay the electrophysiological and/or behavioral consequences of manipulating activity in specific subsets of neurons. Identification and characterization of distinct cell types in the sSC, the correlation between cellular and functional properties of cells, and transgenic mice that facilitate manipulations of the output of these specific neurons represents a fundamental step toward overcoming this obstacle.

References

Andermann ML, Kerlin AM, Roumis DK, Glickfeld LL, Reid RC (2011) Functional specialization of mouse higher visual cortical areas. Neuron 72:1025–1039. CrossRef Medline

Ascoli GA, Alonso-Nanclares L, Anderson SA, Barrionuevo G, Benavides-Piccione R, Burkhalter A, Buzsáki G, Cauli B, DeFelipe J, Fairén A, Feldmeyer D, Fishell G, Fregnac Y, Freund TF, Gardner D, Gardner EP, Goldberg JH, Helmstaedter M, Hestrin S, Karube F, et al. (2008) Petilla terminology: nomenclature of features of GABAergic interneurons of the cerebral cortex. Nat Rev Neurosci 9:557–568. CrossRef Medline

Baker SN, Gerstein GL (2001) Determination of response latency and its application to normalization of cross-correlation measures. Neural Comput 13:1351–1377. CrossRef Medline

Barnett PD, Nordström K, O'carroll DC (2007) Retinotopic organization of small-field-target-detecting neurons in the insect visual system. Curr Biol 17:569–578. CrossRef Medline

Berman N, Cynader M (1972) Comparison of receptive-field organization of the superior colliculus in Siamese and normal cats. J Physiol 224:363–389. Medline

Briggman KL, Helmstaedter M, Denk W (2011) Wiring specificity in the direction-selectivity circuit of the retina. Nature 471:183–188. CrossRef Medline

Callaway EM (1998) Local circuits in primary visual cortex of the macaque monkey. Annu Rev Neurosci 21:47–74. CrossRef Medline

Chalupa LM, Thompson I (1980) Retinal ganglion cell projections to the superior colliculus of the hamster demonstrated by the horseradish peroxidase technique. Neurosci Lett 19:13–19. CrossRef Medline

Cowey A (2010) The blindsight saga. Exp Brain Res 200:3–24. CrossRef Medline

Dean P (1981) Grating detection and visual acuity after lesions of striate cortex in hooded rats. Exp Brain Res 43:145–153. Medline

Dräger UC, Hubel DH (1975) Responses to visual stimulation and relationship between visual, auditory, and somatosensory inputs in mouse superior colliculus. J Neurophysiol 38:690–713. Medline

Edwards MD, White AM, Platt B (2002) Characterisation of rat superficial superior colliculus neurones: firing properties and sensitivity to GABA. Neuroscience 110:93–104. CrossRef Medline

Endo T, Yanagawa Y, Obata K, Isa T (2003) Characteristics of GABAergic neurons in the superficial superior colliculus in mice. Neurosci Lett 346:81–84. CrossRef Medline

Endo T, Tarusawa E, Notomi T, Kaneda K, Hirabayashi M, Shigemoto R, Isa T (2008) Dendritic Ih ensures high-fidelity dendritic spike responses of motion-sensitive neurons in rat superior colliculus. J Neurophysiol 99:2066–2076. CrossRef Medline

Friedlander MJ (1982) Structure of physiologically classified neurones in the kitten dorsal lateral geniculate nucleus. Nature 300:180–183. CrossRef Medline

Friedlander MJ, Lin CS, Sherman SM (1979) Structure of physiologically identified X and Y cells in the cat's lateral geniculate nucleus. Science 204:1114–1117. CrossRef Medline

Friedlander MJ, Lin CS, Stanford LR, Sherman SM (1981) Morphology of functionally identified neurons in lateral geniculate nucleus of the cat. J Neurophysiol 46:80–129. Medline

Gerfen CR, Paletzki R, Heintz N (2013) GENSAT BAC cre-recombinase driver lines to study the functional organization of cerebral cortical and basal ganglia circuits. Neuron 80:1368–1383. CrossRef Medline

Gilbert CD, Wiesel TN (1979) Morphology and intracortical projections of functionally characterised neurones in the cat visual cortex. Nature 280:120–125. CrossRef Medline

Glickfeld LL, Histed MH, Maunsell JH (2013) Mouse primary visual cortex is used to detect both orientation and contrast changes. J Neurosci 33:19416–19422. CrossRef Medline

Harris JA, Oh SW, Zeng H (2012) Adeno-associated viral vectors for anterograde axonal tracing with fluorescent proteins in nontransgenic and cre driver mice. Curr Protoc Neurosci Chapter 1:Unit 1.20.1–18. CrossRef Medline

Hubert L, Arabie P (1985) Comparing partitions. J Classification 2:193–218. CrossRef

Ko H, Hofer SB, Pichler B, Buchanan KA, Sjöström PJ, Mrsic-Flogel TD (2011) Functional specificity of local synaptic connections in neocortical networks. Nature 473:87–91. CrossRef Medline

Koehler CL, Akimov NP, Rentería RC (2011) Receptive field center size

decreases and firing properties mature in ON and OFF retinal ganglion cells after eye opening in the mouse. J Neurophysiol 106:895–904. CrossRef Medline

Krauzlis RJ, Lovejoy LP, Zénon A (2013) Superior colliculus and visual spatial attention. Annu Rev Neurosci 36:165–182. CrossRef Medline

Langer TP, Lund RD (1974) The upper layers of the superior colliculus of the rat: a Golgi study. J Comp Neurol 158:405–435. CrossRef

Leopold DA (2012) Primary visual cortex: awareness and blindsight. Annu Rev Neurosci 35:91–109. CrossRef Medline

Livingstone M, Hubel D (1988) Segregation of form, color, movement, and depth: anatomy, physiology, and perception. Science 240:740–749. CrossRef Medline

Lo FS, Cork RJ, Mize RR (1998) Physiological properties of neurons in the optic layer of the rat's superior colliculus. J Neurophysiol 80:331–343. Medline

Luksch H, Khanbabaie R, Wessel R (2004) Synaptic dynamics mediate sensitivity to motion independent of stimulus details. Nat Neurosci 7:380–388. CrossRef Medline

Madisen L, Zwingman TA, Sunkin SM, Oh SW, Zariwala HA, Gu H, Ng LL, Palmiter RD, Hawrylycz MJ, Jones AR, Lein ES, Zeng H (2010) A robust and high-throughput Cre reporting and characterization system for the whole mouse brain. Nat Neurosci 13:133–140. CrossRef Medline

May PJ (2006) The mammalian superior colliculus: laminar structure and connections. Prog Brain Res 151:321–378. CrossRef Medline

McIlwain JT, Buser P (1968) Receptive fields of single cells in the cat's superior colliculus. Exp Brain Res 5:314–325. Medline

Merigan WH, Maunsell JH (1993) How parallel are the primate visual pathways? Annu Rev Neurosci 16:369–402. CrossRef Medline

Mize RR (1988) Immunocytochemical localization of gamma-aminobutyric acid (GABA) in the cat superior colliculus. J Comp Neurol 276:169–187. CrossRef Medline

Mooney RD, Nikoletseas MM, Ruiz SA, Rhoades RW (1988) Receptive-field properties and morphological characteristics of the superior collicular neurons that project to the lateral posterior and dorsal lateral geniculate nuclei in the hamster. J Neurophysiol 59:1333–1351. Medline

Mysore SP, Knudsen EI (2011) The role of a midbrain network in competitive stimulus selection. Curr Opin Neurobiol 21:653–660. CrossRef Medline

Nassi JJ, Callaway EM (2009) Parallel processing strategies of the primate visual system. Nat Rev Neurosci 10:360–372. CrossRef Medline

Nordström K, O'Carroll DC (2009) Feature detection and the hypercomplex property in insects. Trends Neurosci 32:383–391. CrossRef Medline

Nover H, Andersen CH, DeAngelis DC (2005) A logarithmic, scale-invariant representation of speed in the macaque middle temporal area accounts for speed discrimination performance. J Neurosci 25:10049–10060. Medline

O'Leary DD, McLaughlin T (2005) Mechanisms of retinotopic map development: Ephs, ephrins, and spontaneous correlated retinal activity. Prog Brain Res 147:43–65. CrossRef Medline

Perry VH, Cowey A (1984) Retinal ganglion cells that project to the superior colliculus and pretectum in the macaque monkey. Neuroscience 12:1125–1137. CrossRef Medline

Perry VH, Oehler R, Cowey A (1984) Retinal ganglion cells that project to the dorsal lateral geniculate nucleus in the macaque monkey. Neuroscience 12:1101–1123. CrossRef Medline

Petreanu L, Mao T, Sternson SM, Svoboda K (2009) The subcellular organization of neocortical excitatory connections. Nature 457:1142–1145. CrossRef Medline

Priebe NJ, Cassanello CR, Lisberger SG (2003) The neural representation of speed in macaque area MT/V5. J Neurosci 23:5650–5661. Medline

Priebe NJ, Lisberger SG, Movshon JA (2006) Tuning for spatiotemporal frequency and speed in directionally selective neurons of macaque striate cortex. J Neurosci 26:2941–2950. CrossRef Medline

Rand WM (1971) Objective criteria for the evaluation of clustering methods. J Am Stat Assoc 66:846–850. CrossRef

Ringach DL, Shapley RM, Hawken MJ (2002) Orientation selectivity in macaque V1: diversity and laminar dependence. J Neurosci 22:5639–5651. Medline

Sagdullaev BT, McCall MA (2005) Stimulus size and intensity alter fundamental receptive-field properties of mouse retinal ganglion cells in vivo. Vis Neurosci 22:649–659. CrossRef Medline

Schiller PH, Stryker M (1972) Single-unit recording and stimulation in superior colliculus of the alert rhesus monkey. J Neurophysiol 35:915–924. Medline

Schneider GE (1969) Two visual systems. Science 163:895–902. CrossRef Medline

Shapley R (1990) Visual sensitivity and parallel retinocortical channels. Annu Rev Psychol 41:635–658. CrossRef Medline

Sholl DA (1953) Dendritic organization of neurons in the visual and motor cortices of the cat. J Anat 87:387–406. Medline

Taniguchi H, He M, Wu P, Kim S, Paik R, Sugino K, Kvitsani D, Fu Y, Lu J, Lin Y, Miyoshi G, Shima Y, Fishell G, Nelson SB, Huang ZJ (2011) A resource of Cre driver lines for genetic targeting of GABAergic neurons in cerebral cortex. Neuron 71:995–1013. CrossRef Medline

Tohmi M, Meguro R, Tsukano H, Hishida R, Shibuki K (2014) The extrageniculate visual pathway generates distinct response properties in the higher visual areas of mice. Curr Biol 24:587–597. CrossRef Medline

Vaney DI, Peichl L, Wässle H, Illing RB (1981) Almost all ganglion cells in the rabbit retina project to the superior colliculus. Brain Res 212:447–453. CrossRef Medline

Wang L, Sarnaik R, Rangarajan K, Liu X, Cang J (2010) Visual receptive field properties of neurons in the superficial superior colliculus of the mouse. J Neurosci 30:16573–16584. CrossRef Medline

Wang Q, Henry AM, Harris JA, Oh SW, Joines KM, Nyhus J, Hirokawa KE, Dee N, Mortrud M, Parry S, Ouellette B, Caldejon S, Bernard A, Jones AR, Zeng H, Hohmann JG (2014) Systematic comparison of adeno-associated virus and biotinylated dextran amine reveals equivalent sensitivity between tracers and novel projection targets in the mouse brain. J Comp Neurol 522:1989–2012. CrossRef Medline

Weiskrantz L (2009) Is blindsight just degraded normal vision? Exp Brain Res 192:413–416. CrossRef Medline

Wurtz RH, Albano JE (1980) Visual-motor function of the primate superior colliculus. Annu Rev Neurosci 3:189–226. CrossRef Medline

Zhao S, Ting JT, Atallah HE, Qiu L, Tan J, Gloss B, Augustine GJ, Deisseroth K, Luo M, Graybiel AM, Feng G (2011) Cell type-specific channelrhodopsin-2 transgenic mice for optogenetic dissection of neural circuitry function. Nat Methods 8:745–752. CrossRef Medline